Earth and Planetary Science Letters 403 (2014) 188–198

Contents lists available at ScienceDirect

Earth and Planetary Science Letters

www.elsevier.com/locate/epsl

New crater calibrations for the lunar crater-age chronology

Stuart J. Robbins

Laboratory for Atmospheric and Space Physics, University of Colorado at Boulder, 3665 Discovery Dr., Boulder, CO 80309, United States

ARTICLE INFO

Article history:
Received 14 May 2013
Received in revised form 13 June 2014
Accepted 24 June 2014
Available online 21 July 2014
Editor: C. Sotin

Keywords:
Moon
craters
lunar chronology
lunar history

ABSTRACT

Measuring the spatial density of craters emplaced on geologic units is the primary method used for remotely estimating ages of solar system surfaces. The calibration for this method, which enables conversion of crater density to absolute age, comes from *Apollo* and *Luna* lunar samples for which absolute radiometric ages have been determined. Researchers throughout the 1970s worked to establish the lunar chronology system based on that calibration, correlating crater densities with absolute ages. However, no uniform crater study has been conducted on all calibration terrains, a limitation that was previously unaddressed until this study. The latest lunar images from the *Lunar Reconnaissance Orbiter* were used here to re-map the eleven main sampling sites and new crater counts of those surfaces were conducted. These show significant differences for many sites' crater counts, in many cases having more craters than previously identified. These results, calibrated to the radiometric ages, show a revised lunar crater chronology that changes previously established crater-based ages by up about 1 billion years: Surfaces younger than ~3.6 Gyr and older than ~3.9 Gyr under the classic chronology are younger in this system, and those in-between are older in this new system.

1. Introduction

Craters are ubiquitous across nearly every solid surface in the solar system, and they have long been used as a metric for assigning relative ages: If a surface has more craters of a given size per unit area, then it is older because crater accumulation is temporally cumulative. Assigning absolute ages based on these crater counts requires calibrating a given crater density with a known surface age. Since the Moon represents a more ancient surface than Earth and *Apollo* astronauts and *Luna* craft returned samples that could be radiometrically dated, crater chronologies are based on the Moon. With such a model for the bombardment history at the Moon, one can use dynamical models for different bombardment rates of asteroids and comets on other planets to determine crater-based model ages across the rest of the inner solar system.

Almost all work upon which our current timescales are based was done in the 1970s using early satellite and *Apollo* photographs (Greeley and Gault, 1970; Shoemaker et al., 1970a, 1970b; Soderblom and Boyce, 1972; Neukum et al., 1975; Neukum and Horn, 1976; König, 1977; Moore et al., 1980; Neukum, 1983; Wilhelms, 1987; Neukum and Ivanov, 1994). Crater-based chronology is usually represented as the total number of craters with diameters $\geq$1 km per one or one million km^2 versus an absolute age; this crater density is denoted $N(1)$. The majority of age calibration points are from lunar mare (dark lava flood plains), two are from older lunar highlands, and five are tied to relatively young, individual craters, including three directly at the landing sites. These crater counts have been reexamined in part since recent imagery has been available and with a modern understanding of impactor dynamics, asteroid populations, and secondary cratering (Hartmann et al., 2007; Marchi et al., 2009; Hiesinger et al., 2012). The present study employs modern, uniform, high spatial resolution imagery to directly measure the $N(1)$ calibration points on surfaces of known ages that include $N(1)$ to perform the first uniform study of all calibration sites.

2. Methods

There have been no published geologic maps of the spacecraft landing sites since those from the *Apollo* Preliminary Science Reports (e.g., Shoemaker et al., 1969). These were based on early spacecraft, telescopic, and *Apollo* photographic data. Beyond these, other coarse maps were published that showed areas on which craters were measured (Greeley and Gault, 1970; Neukum et al., 1975), though the number of sites is limited in both; one recent study (Hiesinger et al., 2012) showed the small patches on which they identified craters. Consequently, the first step of this work was to examine the landing sites and map a single unit per site upon which craters could be identified, and all steps are summarized in Fig. 1.

E-mail address: stuart.robbins@colorado.edu.

http://dx.doi.org/10.1016/j.epsl.2014.06.038
0012-821X/

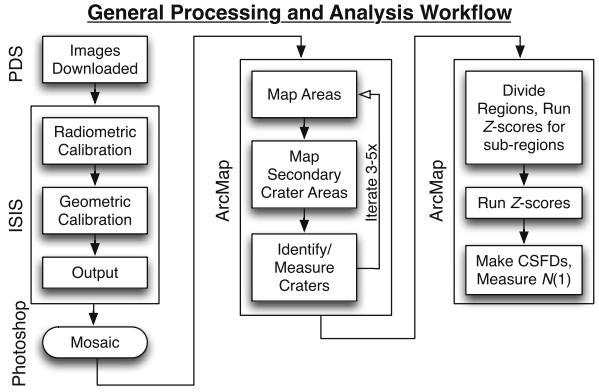

Fig. 1. Processing and analysis workflow (described in detail in Section 2). All images were downloaded from PDS and processed in ISIS. WAC images only were mosaicked in Photoshop. All mapping, crater identification, measurement was conducted in ArcMap, and then density and Z-statistic tests were run on each region and sub-regions within each region to verify they were homogeneous. Final analysis was conducted in Igor Pro software.

Images used were from the *Lunar Reconnaissance Orbiter* Camera Wide- and Narrow-Angle Camera (LROC WAC and NAC) obtained via the Planetary Data Systems (PDS) online interface, processed via standard techniques in Integrated Software for Imagers and Spectrometers (ISIS), and output in the lunar coordinate system. Images were taken at a solar incidence angle of ~58° and ~83° for all landing sites and WAC were manually assembled at a scaled 60 m/px in Adobe Photoshop to eliminate banding, lighting mismatches, and other artifacts that tend to result from automated mosaicking. While higher resolution imagery does exist for many sites, they were not used because the smallest features identified in this work were on the scale of ~500 m. NAC images were used for three small-crater calibration sites and were not mosaicked.

Mapping was conducted via standard geomorphologic techniques (Hare et al., 2009) with both imagery and topography data; an emphasis was placed on being conservative – eliminating any feature that could possibly be of a different unit or make crater identification more difficult (e.g., small massifs, graben, wrinkle ridges, rilles, large (>10 km) craters and associated ejecta). Unit boundaries were based on geologic contacts, linear geologic features, edges of mosaics, and lines of latitude or longitude to be roughly symmetric about the landing site (where applicable). Each mapped region was searched for morphologically distinct secondary craters which were also eliminated from the crater identification area; secondary craters were identified based on standard morphologic criteria (Shoemaker, 1962, 1965; Oberbeck and Morrison, 1974; McEwen and Bierhaus, 2006; Robbins and Hynek, 2014), but it is possible that non-morphologically obvious secondaries were not excluded (i.e., random background secondary craters that look like primary craters). The possibility of contamination by non-uniform random background secondary craters is discussed in the Supplementary material Section 2 and shown to be unlikely.

Accurate measurement of the area of mapped regions is important because crater counts are normalized to area. Areas were calculated in ArcMap via a Mollweide equal-area projection with false northing and central meridian at the center of each mapped region. The areas of regions of secondary craters were removed from the overall unit.

Craters with diameters $D \approx 0.5$–10 km were identified visually (manually) in the mosaics within the mapped regions and measured by tracing their rims, and the three youngest calibration points examined (Cone, North Ray, and South Ray craters) used craters as small as 10 m. The digitized rims were fit by a circle-fitting algorithm that calculates the location and diameter of the craters (Robbins and Hynek, 2012); included unpublished data by C.I. Fassett were measured on similar LROC images within ArcMap using the CraterTools software add-on (see Appendices A and B in Robbins et al., 2014). After this, all regions were arbitrarily sub-divided into two to four sub-regions. Crater density and a Z-statistic for each sub-region (and each overall region) were calculated to ensure uniformity (the same crater density as the overall region) and non-clustering. The Z-statistic is the number of standard deviations by which a Poisson distribution (which primary craters should follow) deviates from randomness and has been used to examine crater spatial distributions in the past (e.g., Clark and Evans, 1954; Squyres et al., 1997). In all cases in this study, the sub-region crater densities were within the uncertainty of the other sub-regions from the same site and the overall region itself, and the Z-statistic indicated that the null hypothesis – that the craters were spatially random – was not rejected.

In dating surfaces, the most common technique is to create a size-frequency distribution (SFD) which is a histogram of crater diameters (Crater Analysis Techniques Working Group, 1979). The histogram is summed from large to small diameters to create a cumulative version (CSFD), and this is divided by the area on which craters were identified. This was done for all sites, but instead of binning the CSFD, a ranked histogram was created so as to best represent the data. A ranked histogram is where craters are sorted from largest to smallest, the diameter placed on the abscissa, and the order in the list on the ordinate axis; this avoids the smoothing inherent in any binning system. The $N(1)$ data point was then read from the CSFDs in 7 of the 11 regions considered; in four cases, other techniques were used due to the small region mapped or empirical crater saturation at $D = 1$ km, discussed below. All sites' maps and CSFDs are shown in Figs. 3–5 (and high-resolution maps are included as online supplemental data). Three significant figures for the crater counts from this work are shown while others are listed to the precision found in the original papers.

3. Calibration sites

This section discusses each of the 11 calibration sites used with details of mapping, crater counts, and comparison with previous work. Figs. 3–5 show the mapping and crater counts. Three sites (*Apollo 15, 16*, and *Luna 24*) have historic maps available, and detailed comparisons are made in the supplemental material. Additional calibration details are also discussed in the supplemental material, including consistency tests to determine if secondary crater contamination was significant.

3.1. Apollo 11

Mare Tranquilitatis is ~6 million km^2, while the mapped region in this study around the lunar module *Eagle* is 13,892 km^2. The maria surrounding the lander appears homogenous with no obvious distinct units. The mapped region is bound by the limits of the WAC strips used to the north, the wrinkle ridge east of Sabine crater to the west, a series of grabens to the south, and a wrinkle ridge and 25.615° east (border of WAC strip); the region is roughly centered on Collins crater. This region is heavily contaminated by secondary craters and an area 1064 km^2 was removed to eliminate these, yielding a final area of 12,828 km^2. The results and literature comparisons are:

- $N(1) = 8140 \pm 800$ per 10^6 km^2 (this work)
- $N(1) = 4900 \pm 700$ (Fassett, pers. comm.)
- $N(1) = 9000 \pm 1800$ (Neukum and Ivanov, 1994)
- $N(1) = 9300$–9357 (Marchi et al., 2009, fitting data from Neukum, 1983)
- $N(1) \approx 9120$ (Shoemaker et al., 1970b)
- $N(1) \approx 12{,}900$ (Shoemaker et al., 1970a)